# Postweld Heat Treatment of 15Cr-6Ni-2Mo-1Cu Supermartensitic Stainless Steel Welds

## A design guide enables optimization of PWHT for heat-affected zone hardness reduction with preservation of base metal yield strength

BY R. E. BAUMER, E. C. P. PESSOA, K. KRISHNAN, AND T. N. VU


## Abstract

Supermartensitic stainless steels with 15Cr-6Ni-2Mo-1Cu and 135 ksi minimum yield strength (15Cr-135 SMSS) offer high strength and good toughness through a complex hierarchical microstructure of nanoscale precipitates, tempered martensite, and reverted austenite. Upon welding and postweld heat treatment, substantial changes to heat-affected zone microstructure and hardness may occur. Here, we reveal spatially heterogeneous microstructure and microhardness in the HAZ of 15Cr-135 SMSS; correlate these changes to measured phase transformation temperatures; and demonstrate that HAZ hardness changes depend strongly on postweld heat treatment (PWHT) temperatures. Furthermore, we demonstrate that PWHT may lead to undesired reductions in base metal yield strength and formulate a design guide for PWHT that quantifies the trade-offs in desired reductions of HAZ hardness with undesired changes to base metal yield strength. These findings have important practical implications for welding procedure design and qualification.



## Keywords

- Supermartensitic Stainless Steel
- Gas Tungsten Arc Welding
- Reverted Austenite
- Design Guide
- Postweld Heat Treatment


## Introduction

Supermartensitic stainless steel (SMSS) alloys offer a balance of intermediate corrosion resistance (Refs. 1, 2), high strength (Refs. 1, 3), and good weldability (Refs. 4–6), which is attractive for sour service oil and gas applications (Refs. 7, 8). Alloys with nominal compositions of 13Cr-5Ni-2Mo and less than 0.03 wt-% C typically have minimum yield strengths between 95 ksi or 110 ksi, with yield strength depending upon heat treatment condition and fraction of retained austenite (Refs. 1–3). More recently, SMSS alloys with 15Cr-6Ni-2Mo-1Cu (UNS S42625) have been developed that have improved corrosion resistance and higher yield strength compared to 13Cr SMSS alloys (Ref. 9). 15Cr SMSS are important to industry due to higher strength and superior corrosion resistance compared to conventional 13Cr SMSS, as well as being less expensive than duplex stainless steels (Refs. 9–10). For welded SMSS components to resist corrosion-related failures (Ref. 11), such as stress chloride cracking (SCC) or sulfide stress cracking (SSC), microstructure and hardness in the base metal, fusion zone (FZ), and heat-affected zone (HAZ) must be controlled. The FZ (Refs. 4–6, 12), HAZ (Refs. 13, 14), and postweld heat treatment (PWHT) response (Refs. 7, 8, 14) of 13Cr SMSS alloys have been well studied. Here, we extend our previous work on the weldability 13Cr SMSS alloys (Ref. 14) to quantify the HAZ response of 135 ksi minimum yield strength 15Cr SMSS alloys.

## Background

The 13Cr and 15Cr SMSS alloys are designed to be martensitic upon quenching (Refs. 2, 10). However, to improve toughness and reduce base metal hardness (Ref. 1, 15), post-quench tempering in an intercritical range between the austenite start ($A_1$) and finish ($A_3$) temperatures may be used to form reverted austenite (Ref. 15) without a loss of corrosion resistance (Refs. 1, 10). Intercritical heat treatment in 13Cr SMSS alloys has been successfully optimized to control the amount of reverted austenite (Ref. 16–18), which is stable due to the high-temperature partitioning of Ni into reverted austenite and lowering of martensite start temperature below room temperature (Ref. 12). To avoid in-service failure in welded SMSS, standards such as NACE

https://doi.org/10.29391/2024.103.022

MR0175/ISO 15156 specify HAZ hardness limits, which are intended to avoid in-service cracking due to stress sulfide cracking (SSC) (Ref. 19). While 13Cr SMSS alloys typically have carbon content below 0.03 wt-%, as-welded HAZ hardness may still exceed specified limits and require PWHT (Refs. 7, 11, 20). While PWHT can be designed to reduce HAZ hardness in 13Cr SMSS, it may result in undesired reductions in base metal yield strength (Ref. 14). 15Cr SMSS alloy is an interesting alternative due to higher yield strength and superior corrosion resistance in more severe environments with $CO_2$ and $H_2S$ (Refs. 9, 10). It is therefore of great interest to understand the response of 15Cr SMSS alloy to both welding and PWHT.

## Literature Review

To date, studies on 15Cr SMSS alloys have focused on heat treatment (Ref. 21) and corrosion response (Refs. 9, 10), but the weldability has received little investigation. Ishiguro et al. investigated the impact of austenite fraction on the corrosion response of a 15Cr-6Ni-2Mo-1Cu alloy and a 17% Cr alloy, showing a significant change in the fraction of reverted austenite for tempering at temperatures of 565 °C to 615 °C (Ref. 10). While they report that the increased fraction of austenite does not change corrosion resistance, it does correlate to a significant drop in yield strength from 145 to 123 ksi (Ref. 10). Barbosa et al. show that tempering of a 15Cr-5.8Ni-1.9Mo-1Cu alloy with temperatures between 550 °C to 600 °C results in a marked increase in austenite volume fraction which is accompanied by a hardness reduction of 400 HV10 to 315 HV10 for tempering temperatures of 500 °C and 650 °C, respectively (Ref. 21). Similarly, Ye et al. show a reduction in hardness of approximately 34 HRC to 27.5 HRC with tempering temperatures of 600 °C and 650 °C in a 14.8Cr-6.5Ni-2Mo-1.4Cu-0.8W-0.021C alloy (Ref. 22). In follow-up work characterizing a 14.8Cr-6.5Ni-1.8Mo-1.45Cu-0.021C alloy (Ref. 23), Ye et al. calculate the equilibrium phase diagram, measure the fraction of austenite in the solution annealed and oil-quenched condition, as well as after annealing, and conclude that the $A_1$ temperature is below 550 °C. Together, these studies suggest that the $A_1$ temperature is in the range of 550 °C to 615 °C (Refs. 10, 21–23), but more work is needed to quantify phase transformation temperatures, and the dependence of transformation temperatures on heating rate (Ref. 24) and its relationship to PWHT response (Ref. 14).

In addition to the presence of retained and reverted austenite with tempered martensite (Refs. 1, 10, 21, 22), previous investigations of the 15Cr SMSS alloy system have revealed the presence of delta ferrite (Ref. 21) and nanoscale Cu-rich precipitates (Refs. 22, 23). Kimura et al. reports that the quenched and tempered 15Cr-6Ni-2Mo-1Cu alloy has a microstructure with precipitates, although the precipitate phase/composition is not reported (Ref. 9). Ye et al. demonstrate that the addition of Cu to a 15Cr alloy (15Cr-6.5Ni-2Mo-1.5Cu-0.8W-0.02C) promotes the formation of austenite and increases ultimate tensile strength after tempering due to the formation of nanoscale phase Cu-rich precipitates that are 20–50 nm diameter (Ref. 22). Ye et al. report similar results in an alloy without W (Ref. 23). Zhou et al. have shown through microstructural characterization and micromechanical modeling of the 15.7Cr-4.9Ni-0.4Mo-3.3Cu-0.028C system that tempering at 500 °C changes dislocation density, precipitate fraction, and martensite lath size, leading to changes in material yield strength (Ref. 25). Finally, nanoscale precipitates have also been reported in 15-5PH stainless steel alloys, such as reported by Couturier et al. (Ref. 26). These prior investigations suggest that the 15Cr-135 SMSS alloy may display significant metallurgical changes in the heat-affected zone both in the as-welded condition and following PWHT. To our knowledge, no published study has yet investigated the HAZ microstructure in this alloy.

## Objective

In this paper, we resolve these gaps by quantifying the heat-affected zone hardness in 135 ksi minimum yield strength 15Cr-6Ni-2Mo-1Cu supermartensitic stainless steel alloy (hereafter, abbreviated 15Cr-135 SMSS) and measuring the dependence of HAZ hardness on postweld heat treatment peak temperature. Additionally, we demonstrate that PWHT can have a significant impact on base metal yield strength. Using a combination of heat treatment and welding experiments, we developed a design guide showing the optimal process parameters for controlling heat-affected zone hardness while minimizing the reduction of base metal yield strength. Finally, microstructure evolution with PWHT temperature is correlated to HAZ properties and base metal yield strength. The design guide methodology may be useful for quantifying the PWHT response of other martensitic alloys.

## Experimental Procedures

### Materials

Supermartensitic stainless steel 15Cr-135 tubing with an outer diameter of 4.500 in (114.3 mm) and a nominal wall thickness of 0.436 in (11.07 mm) was investigated, with the material test report (MTR) indicating a nominal 15Cr-6Ni-2Mo-1Cu composition (see Table 1) and quenched and tempered (575°C ± 10 °C) heat treatment condition. Average mechanical properties, based on the MTR, are given in Table 2. The maximum hardness for the 15Cr-135 SMSS alloy (UNS S42625) material is specified by the manufacturer to be 37 HRC, which by ASTM E140 equation A1.1.1 (Ref. 27) is equivalent to 363 HV. The HAZ hardness is targeted to be less than or equal to the base metal hardness.

### Dilatometry

Metallurgical phase transformation temperatures were measured in samples sectioned longitudinally from as-received tubing. Radial displacements at the sample midpoint were measured with a C-gauge type dilatometer during resistive heating, controlled cooling, and force control with a target of $F = 0$ $k$N in a thermomechanical physical simulator (see Fig. 1). Two specimens per condition were instrumented with chromel/alumel K-type 0.010 in. diameter thermocouples and heated at variable linear heating rates of 5, 1, and 0.5 °C $s^{-1}$ to 900 °C and then immediately cooled at 5 °C $s^{-1}$ to

**Table 1 — MTR Reported Chemical Composition of 15Cr-135 SMSS Tubing**

| | C | Si | Mn | P | S | Cr | Ni | Mo | Cu |
|---|---|---|---|---|---|---|---|---|---|
| wt-% | 0.03 | 0.24 | 0.31 | 0.017 | <0.001 | 14.7 | 6.21 | 1.93 | 0.95 |

**Table 2 — Average Mechanical Properties of 15Cr-135 SMSS Tubing Computed from MTR Data**

| Yield Strength (ksi) | Tensile Strength (ksi) | Elongation (%) | Rockwell Hardness (HRC) |
|---|---|---|---|
| 143.5 | 152 | 24.5 | 35.1 ± 0.2 |

room temperature. Phase transformation temperatures were identified through analysis of the C-gauge displacement ($\delta$) versus temperature ($T$), along with its derivative computed from the slope of the best-fit line over a ± 4 °C temperature interval centered at the indicated temperature. Following previous studies (Refs. 14, 28), during heating, changes in the slope of $\delta(T)$ were taken as the onset/completion of the start and finish of the austenite transformation temperatures, $A_1$ and $A_3$, respectively. Upon cooling, the martensite start temperature $M_S$ was likewise identified by the change in slope of $\delta(T)$.

## Gas Tungsten Arc Welding Experiments

Welding coupons of a nominal length of 5 in. and width of 2 in. were sectioned longitudinally from the 15Cr-135 SMSS tubing. The mill scale was removed from the outer (convex) surface by grinding, with the final preparation for welding by grinding with an 80-grit flap wheel. As previously reported (Ref. 14), an autogenous gas tungsten arc (GTA) bead-on-plate (BOP) weld was performed with a mechanized welding system in the longitudinal direction on the coupon with a current of 120 A, voltage of 11.0 volts, and travel speed of 2.64 in./min (nominal heat input of 30 kJ/in.) with 100% argon shielding. Transverse cross-sections (approximately 6–8 mm in thickness) were removed from the autogenous weld for subsequent heat treatment and metallurgical analysis of the heat-affected zones (HAZ).

## Postweld Heat Treatment Experiments

Single cycle postweld heat treatment (PWHT) experiments were performed with transverse weld cross-sections with a 1 h soak at target temperatures varying from 552 °C to 661 °C (1025 °F to 1225 °F in 25 °F increments), with target heating and cooling rates of 0.0567 °C $s^{-1}$ in a programmable furnace. Heating rates were similar to the maximum postweld heat treatment heating rate of 400 °F/hr specified in ASME Section VIII (0.062 °C $s^{-1}$) (Ref. 29). The target peak temperatures for the single cycle PWHT experiments were selected based on data previously reported by Ishiguro and shown to result in reverted austenite upon tempering of austenitized/quenched 15Cr-135 SMSS alloy (Ref. 10). In-situ temperature measurements with an external data acquisition system revealed that the actual soak temperatures were on average 4.0 °C lower than the target peak temperature. Therefore, for simplicity, target peak temperatures are utilized for subsequent analysis.

## Metallography

Weld specimens, in the as-welded and PWHT conditions, were cross-sectioned transverse to the welding direction and mounted for metallurgical analysis. Representative base metal samples were sectioned transverse to the longitudinal tubing axis, in the same cross-section orientation as the welded samples. Mounted samples were ground and polished to 1.0 µm using standard metallurgical procedures and then etched with Kalling's No. 1 etchant (33 ml $H_2O$, 33 HCl, 33 ethanol, 1.5 g $CuCl_2$, see [Ref. 2]) for 15 to 35 s. Selected specimens were studied with macro imaging, optical microscopy, and tungsten filament scanning electron microscopy (SEM).

## Microhardness Testing

Vickers microhardness measurements were performed with a 500 g load and a 15 s dwell time, following ASTM E384 standard (Ref. 30), using measurements in three different locations. First, as shown with the macro image in Fig. 2A, selected specimens were analyzed with microhardness traverses in a zig-zag pattern on a line approximately 0.5 mm below and parallel to the coupon surface, from just inside the FZ to 5 mm from the FZ boundary. The distance between indentations in the same line was approximately 0.25 mm and the distance between lines was approximately 0.1 mm. As indicated in Fig. 2A, the microhardness traverse was repeated on both the right and left sides of the coupon. The results from the right and left sides were averaged.

Second, the impact of PWHT on the HAZ properties was systematically characterized in all specimens by measuring the average hardness in the coarse grain HAZ (CGHAZ) and the edge of the HAZ. As shown in Fig. 2B, microhardness was measured in the CGHAZ with six indents (numbered 4 to 9) located approximately 0.25 mm from the FZ boundary. An additional six indents (three on each side of the sample and numbered 1–3 and 10–12) were located at 4.0 mm from the FZ boundary, as schematically indicated in Fig. 2B.

Third, the impact of PWHT on the base metal properties was systematically characterized in all specimens by mea-

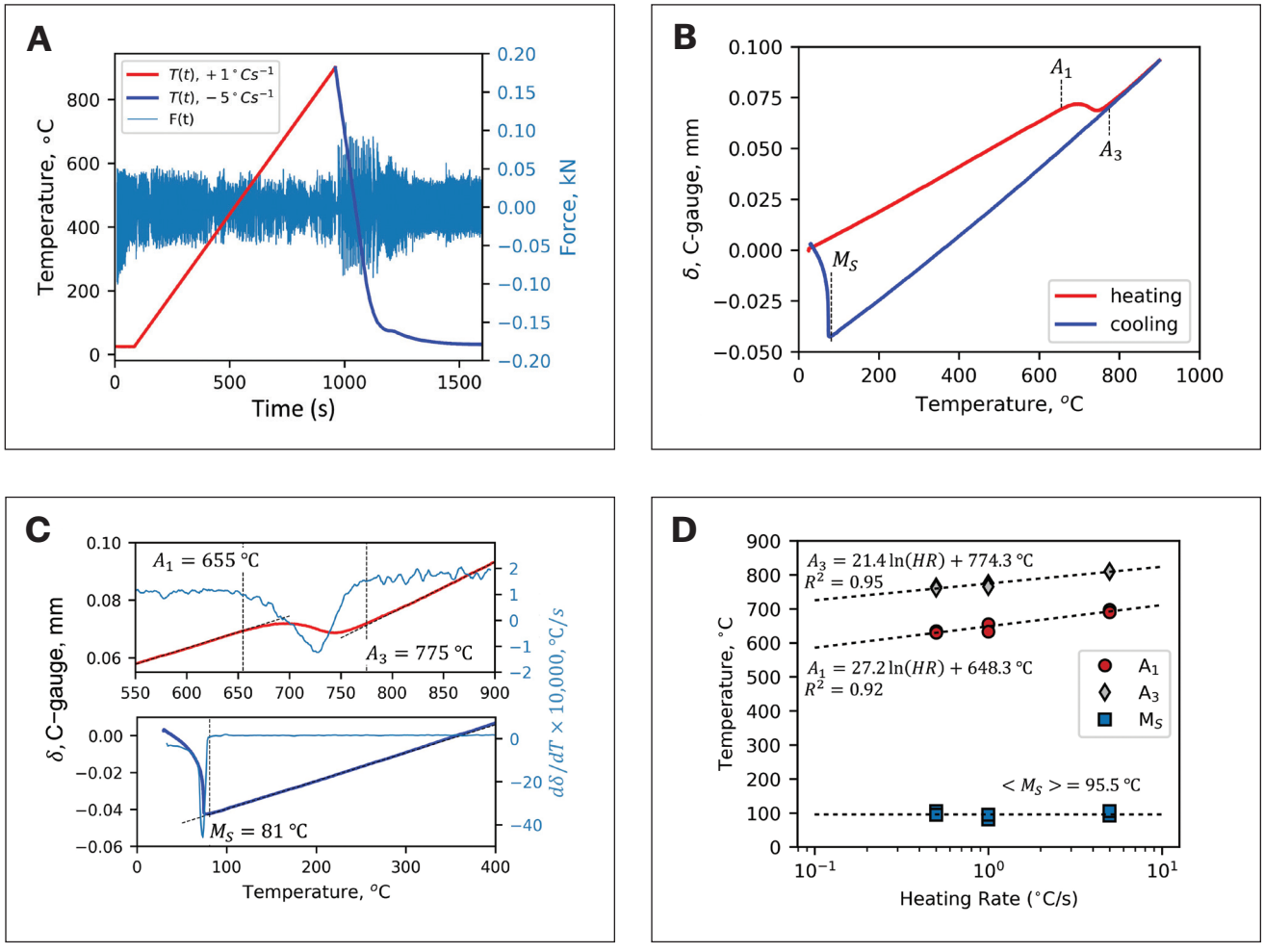


*Fig. 1 — Dilatometry-based determination of the metallurgical phase transformation temperatures using Gleeble®-1500 with C-gauge dilatometer. A — Controlled heating (red) and cooling (thick blue line) under nominal zero force control (thin blue line, right axis); B — dilatometry radial displacement response plotted versus corresponding temperature during heating (red) and cooling (blue) cycles; C — close-up of $A_1$ to $A_3$ transformation, with derivative (right axis) and martensite start transformation. D — Measured $A_1$, $A_3$, and $M_S$ temperatures plotted as a function of heating rate, with best-fit lines indicated.*

suring the average hardness 13 mm from the FZ boundary and numbered 13 to 15 on the left side and 16 to 18 on the right side of each sample as indicated in Fig. 2B.

## Tensile Testing

Tensile specimens were sectioned longitudinally from the 15Cr-135 SMSS tubing, and tensile properties were measured in 15Cr-15 SMSS tubing in the as-received condition, as well as following single cycle heat treatment at 552, 593, and 621 °C for 1 h and target heating/cooling rates of 0.0567 °C $s^{-1}$. Tensile testing was performed with 0.250 in. (6.4 mm) reduced section diameter samples and 1.0 in. (25.4 mm) gauge length per ASTM A370 (Ref. 31), with two or three specimens tested per condition and the average and standard deviation reported for the ultimate tensile strength, 0.2% offset yield strength, elongation, and reduction of area.

# Results

## Phase Transformation Temperatures

A representative dilatometry experiment for the 15Cr-135 SMSS alloy is presented in Fig. 1A for target heating at 1 °C $s^{-1}$ to 900°C and subsequent cooling at a target rate of –5 °C $s^{-1}$ to room temperature. The experiment had a target force control of 0.0 *k*N, with maximum fluctuations less than ±0.4 *k*N (Fig. 1A, right axis). The radial C-gauge displacement (δ) is plotted versus temperature (*T*) in Fig. 1B. Following the approach reported by Barrick and DuPont (Ref. 28), the $A_1$, $A_3$, and $M_s$ temperatures are determined based on a combined analysis of the slope of δ(T) (Fig. 1C) and its derivative with respect to temperature (Fig. 1C, right axis). As can be seen in the close-up view of Fig. 1B (shown in Fig. 1C), at the 1 °C $s^{-1}$ heating rate, the C-gauge displacement response begins to deviate from the linear fit of the heating response at 655 °C, leading to a decrease in the specimen volume (increase

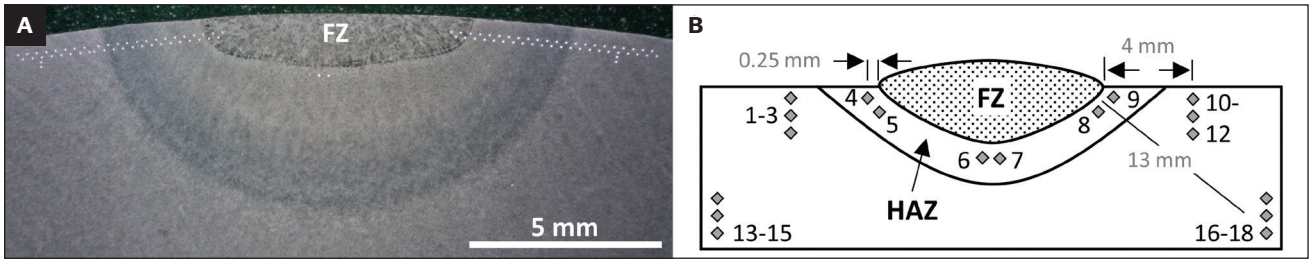


*Fig. 2 — A — Representative cross-section of autogenous gas tungsten arc weld (a-GTAW) performed on 15Cr-135 SMSS coupon followed by postweld heat treatment at 579°C for 1 h. The fusion zone (FZ) is indicated. White reflections are microhardness traverse indentations; B — schematic of microhardness indentation locations (numbered 1–18, see text for explanation).*

**Table 3 — Average Measured Transformation Temperature at Indicated Heating Rate Based on Two Samples**

| Heating Rate (°C $s^{-1}$) | Transformation Temperature, °C | | | |
|---|---|---|---|---|
| | $A_1$ | | $A_3$ | |
| | Avg. | Standard Deviation | Avg. | Standard Deviation |
| 0.5 | 632.5 | 3.5 | 762.5 | 3.5 |
| 1 | 644.0 | 15.6 | 770.0 | 7.1 |
| 5 | 693.5 | 4.9 | 810.0 | 0.0 |

*The error is the standard deviation

in density), consistent with the expected transformation from martensite (body-centered tetragonal structure) to austenite (face-centered cubic structure) and the $A_1$ transformation temperature (Ref. 32). Upon further heating, the slope is again linear in the 800–900 °C range. Analyzing the derivative of C-gauge displacement versus temperature (Fig. 1C), the $A_3$ is taken to be the temperature at which the C-Gauge response is again approximately linear (775 °C in Fig. 1C). Upon cooling from 900 °C, the C-gauge displacement decreases continuously until an abrupt change between further cooling from 100 °C to 25 °C, which is consistent with the expected density decrease associated with the austenite to martensite transformation (Ref. 32). Examining the derivative of the C-gauge displacement versus temperature, the martensite start temperature is found to be $M_S$ = 81 °C (Fig. 1C). Following $M_s$, the C-gauge displacement and its derivative did not reliably indicate the completion of the martensitic phase transformation ($M_F$), suggesting that $M_F$ is below room temperature. In the present experiment, cooling below room temperature was not readily controlled. Therefore, the martensite finish temperature $M_F$ was not measured here.

Additional experiments were performed at heating rates of 5, 1, and 0.5 °C $s^{-1}$ (cooling rate was fixed at 5 °C $s^{-1}$), with two experiments per condition, and analyzed following the method of Fig. 1. The result of each experiment is plotted as an individual data point in Fig. 1D, and the average values are tabulated in Table 3. Consistent with our prior investigation of the 13Cr SMSS system (Ref. 14), the $A_1$ and $A_3$ temperatures are heating rate dependent and fit well by heating rate versus the logarithm of the transformation temperature (Fig. 1D). From Fig. 1D, the following regression equations were obtained: $A_1 = 27.2 \ln(HR) + 648.3$ °C and $A_3 = 21.4 \ln(HR) + 774.3$ °C, where the heating rate (HR) is in units of °C $s^{-1}$, with R-squared fit values of 0.92 and 0.95, respectively. At the applied PWHT heating rates of 0.0567 °C $s^{-1}$, $A_1$ and $A_3$ are predicted to be 570 °C and 713 °C, respectively. The average martensite start temperature is found to be $M_S = 95.5 \pm 9$ °C, which is independent of the heating rate. If prior results $M_F = M_S - 100$ °C (Ref. 2) are representative of this material, $M_F$ may be estimated to be –4.5 °C.

## HAZ Microhardness in 15Cr Welds and Its Correlation to PWHT Condition

A representative macro image of the transverse cross-section of an autogenous GTA BOP weld, followed by single cycle PWHT at 579 °C for 1 h, is presented in Fig. 2A. The fusion zone (FZ) is visible and two distinct zones appear to be present in the heat-affected zone (HAZ) at approximately 1.2 mm and out to 2.6 mm. Since the goal of this study is to correlate the HAZ microstructure and microhardness to PWHT conditions, the FZ is not investigated here. The different HAZ etching

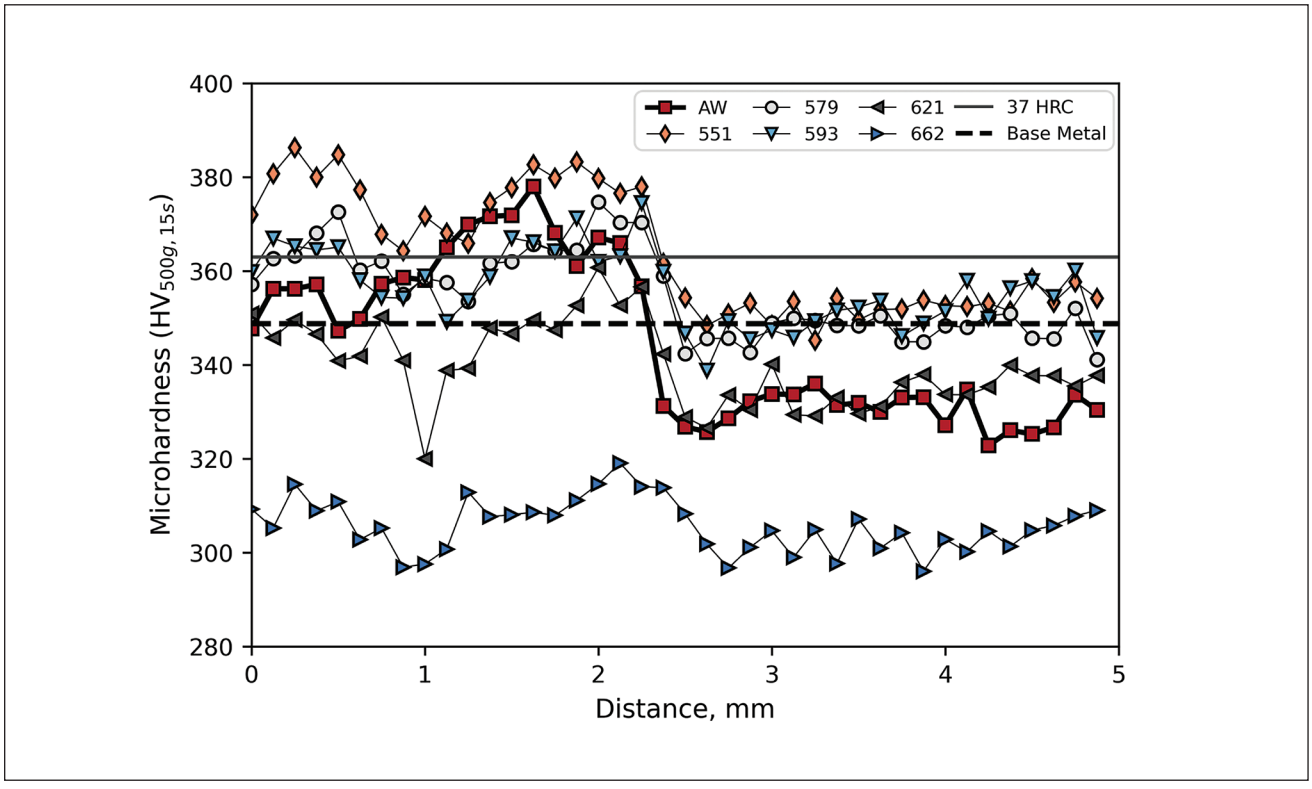


*Fig. 3 — Select microhardness traverse data (average of points on opposite sides, see Fig. 2A) measured in the as-welded (AW) and for PWHT condition of 1 h at 551, 579, 593, 621, and 662°C (temperature indicated in legend). Base metal and target maximum hardness are indicated by thick horizontal dashed and thin solid lines, respectively.*

response in the macro images suggests microstructural heterogeneity in the HAZ. As a first step to test this hypothesis, two microhardness traverses were performed in a zig-zag pattern on opposite sides of the weld (see Fig. 2A).

The as-welded HAZ microhardness traverse result — averaged over the two sides — is presented in Fig. 3 as a thick black line (red square symbols), with results measured after five different PWHT conditions indicated by unique symbols (551, 579, 593, 621, and 662 °C for 1 h, see legend) and a thin black connecting line. Base metal hardness, measured in the same orientation as the weld HAZ, is indicated by the thick dashed black line. For reference, the target maximum HAZ hardness for the material of 37 HRC (363 HV) is indicated as a horizontal thin line. The results in Fig. 3 reveal spatially varying microhardness, with maximum hardness typically found at approximately 0.5 mm and 1.75 mm from the FZ/HAZ boundary, while 1.0 mm shows consistently lower hardness. These results support the visual observation of distinct HAZ zones revealed by macro etching differences (e.g., Fig. 2A).

The HAZ microhardness in the 15Cr-135 SMSS alloy and its correlation to PWHT condition is systematically studied by averaging over six indents approximately 0.25, 4.0, and 13 mm from the FZ boundary, as schematically indicated in Fig. 2B. In Fig. 4, the as-welded microhardness results are presented as a bar chart, with hardness plotted as a function of position from the FZ boundary. In Fig. 4B, the average microhardness is reported for locations approximately 0.25, 4.0, and 13.0 mm from the FZ boundary and plotted as a function of PWHT condition. Additionally, using data from the microhardness traverse data in Fig. 3, the average microhardness value is computed over $0.875 \leq x \leq 1.125$ mm (6 indents total) and $1.5 \leq x \leq 2.0$ mm (10 indents total) from the FZ boundary and plotted as a function of corresponding PWHT condition. As in the case of Fig. 3, in Fig. 4 the base metal average and target maximum HAZ hardness are represented by a thin solid line and a thick dashed line, respectively. The vertical thin dashed line indicates the predicted $A_1 = 570$ °C for the experimental PWHT heating rates of 0.0567 °C $s^{-1}$.

The results in Fig. 4A suggest that in the as-welded condition, the CGHAZ hardness is below the 37 HRC limit (363 HV), but at 1.5–2.0 mm from the FZ, the hardness exceeds the target maximum hardness. Figure 4B shows significant CGHAZ hardening for PWHT below the $A_1$ temperature. For single cycle PWHT at 579, 593, and 607 °C for 1 h (above the $A_1$ temperature), the CGHAZ hardness is found to be approximately equal to the 363 HV (37 HRC) limit (361, 362, and 364 HV, respectively), while the 1.75 mm position is slightly above the target maximum hardness. At PWHT temperatures above 607 °C, the hardness in all HAZ locations decreases, reaching a minimum HAZ hardness of approximately 310 HV at 662 °C PWHT. The base material (13 mm from FZ boundary) hardness is found to be approximately unchanged for PWHT temperatures up to 593 °C, after which a dramatic decrease in base metal hardness is observed, reaching a minimum hardness of 295 HV at 662 °C PWHT.

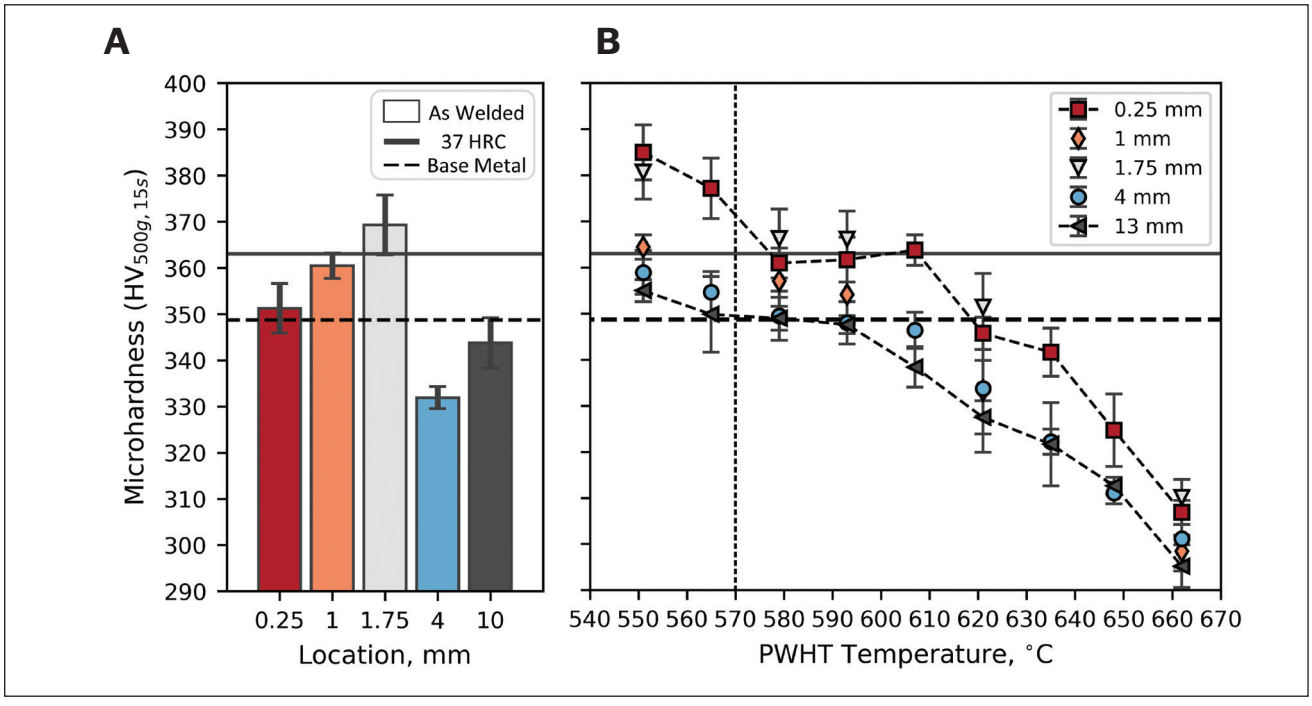


*Fig. 4 — A— Variation of average hardness as a function of distance from FZ boundary in as-welded specimen; B — variation of hardness for weld following postweld heat treatment (PWHT) for 1 h at indicated temperature, binned by different distance from the FZ boundary. Values reported at 1.0 and 1.75 mm were computed from traverse data presented in Fig. 3. The thin, vertical dashed line indicates the predicted $A_1$ = 570°C for the experimental PWHT heating rates of 0.0567 °C $s^{-1}$ (see Fig. 1D). In both (A) and (B), base metal and target maximum hardness are indicated by horizontal dashed and solid lines, respectively, and error bars correspond to ± 1 standard deviation.*

## Correlation of Microstructure to HAZ Position and PWHT Condition in 15Cr Welds

Light optical microscopy of the 15Cr-135 SMSS base metal is presented in Fig. 5A, revealing a fine microstructure consistent with martensite and retained austenite (Ref. 12). The as-welded HAZ microstructure, observed with light optical microscopy at 0.5 mm from the FZ boundary (Fig. 5B), reveals a morphology consistent with an as-quenched martensitic matrix (Ref. 22) expected in the CGHAZ where austenitization, grain growth, and rapid quenching have occurred. Scanning electron microscopy of the base metal at higher magnification (3,000×) (Fig. 5C) reveals the presence of a light etching phase previously reported to be reverted austenite (Refs. 21, 22). By contrast, the as-welded HAZ microstructure, observed with SEM at 0.5 mm from the FZ boundary (Fig. 5D), reveals prior-austenite grain boundaries and morphologies suggestive of martensite (Ref. 22). Figures 5D–F reveal that the fraction of light-etching morphologies — presumed to be austenite — increases with distance (observed at 0.5, 1.0, and 2.0 mm) from the FZ boundary. Consistent with macro imaging (Fig. 2) and microhardness traverse data (Fig. 3), microscopy demonstrates that significant microstructural heterogeneity is present in the HAZ in the as-welded condition (Fig. 5).

Supporting the results of Fig. 4B that demonstrate that the PWHT temperature has a significant impact on the HAZ hardness, significant microstructural changes are observed at 0.5 and 2.0 mm from the FZ boundary for PWHT at 551, 593, and 621 °C (Fig. 6). Comparing the as-welded CGHAZ microstructure (Fig. 5D) to that after PWHT at 551, 593, and 621°C (Figs. 6A–C), increasing fractions of reverted austenite (light-etching phase) are present. At 621°C (Fig. 6C), the morphology qualitatively resembles the base metal microstructure (Fig. 5C). Supporting this observation, the CGHAZ microhardness measured at 621°C is statistically equivalent to the base metal hardness (Fig. 4B). The presence of reverted austenite is pronounced at 2 mm from the FZ boundary at 551 and 593°C (Figs. 6D and E). However, at 621 °C (Fig. 6F) the microstructure is qualitatively distinct, and the intragranular lath-type morphology of reverted austenite is no longer discernable. Furthermore, at 621°C (Fig. 6F), the austenite volume fraction appears to be substantially higher compared to lower temperatures, consistent with the significantly lower HAZ hardness compared to lower PWHT temperatures (Fig. 4B).

## Impact of PWHT on Base Metal Tensile Strength

As previously discussed, notable changes in base metal hardness are observed with increasing PWHT temperature above 593 °C (Fig. 4B). These results suggest that measurable changes to base metal properties, particularly tensile yield strength, may occur above particular PWHT temperatures. Accordingly, the mechanical properties were characterized

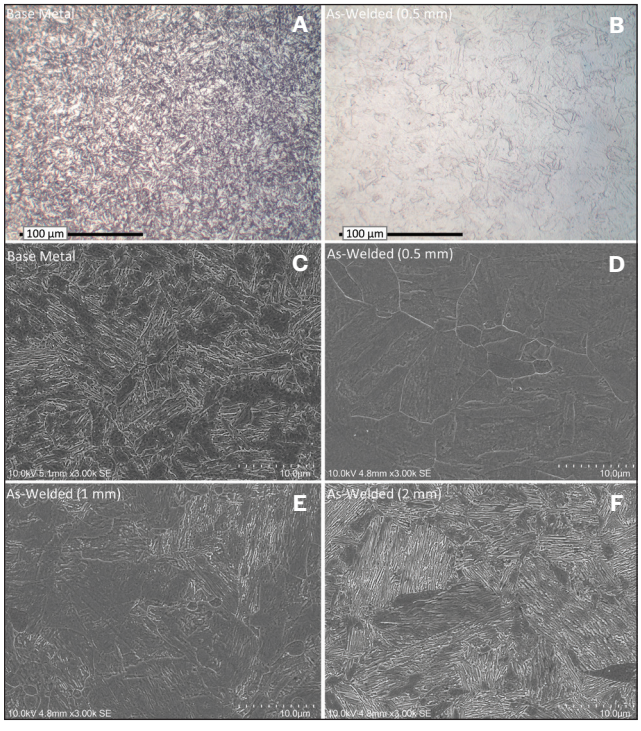


*Fig. 5 — Microscopy of 15Cr-135 SMSS alloy etched with Kalling's No. 1 (see [Ref. 2]). Light optical microscopy of: A — Base metal; B — as-welded 0.5 mm from FZ boundary; C–F — scanning electron microscopy of as-welded 15Cr-135 SMSS alloy at 0.5 below the surface and (D) 0.5 mm, (E) 1.0 mm, and (F) 2.0 mm from the FZ boundary.*

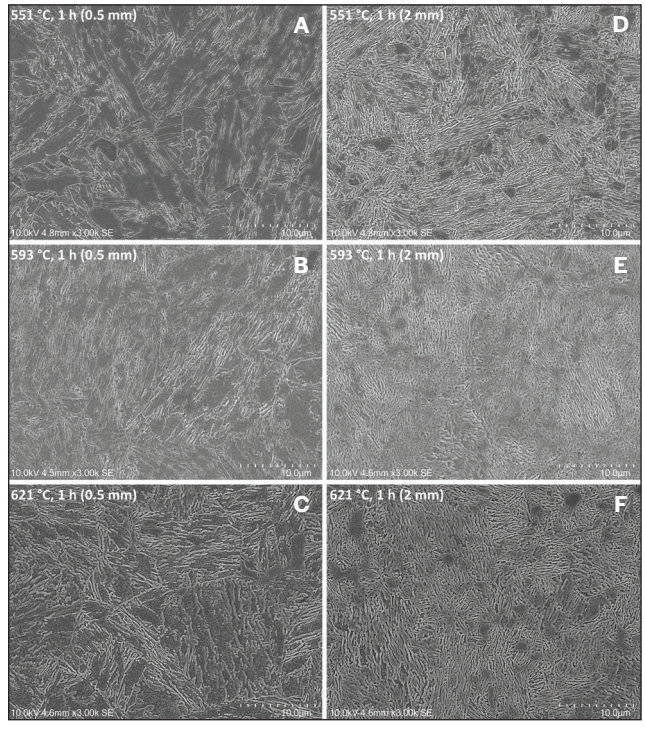


*Fig. 6 — Scanning electron microscopy (3,000×) of 15Cr-135 SMSS weld following postweld heat treatment at 0.5 (A–C) and 2.0 mm (D–F) from the FZ boundary for (A, D) 551°C for 1 h; (B, E) 593°C for 1 h; and (C, F) 621°C for 1 h.*

in base metal samples heat treated at select temperatures (552, 593, and 621 °C) that correspond to select weld PWHT conditions. The mechanical properties are tabulated in Table 4 and the 15Cr-135 SMSS alloy base metal yield strength is plotted as a function of heat treatment peak temperature (fixed 0.0567 °C $s^{-1}$ ramp and cool with 1 h soak at peak temperature) in Fig. 7A. Consistent with the microhardness results (Fig. 4B), at heat treatment temperature above 593°C a significant reduction in base metal yield strength is observed. At 551 °C, no significant change in base metal strength is observed. At 593 °C heat treatment, the average base metal yield strength (138 ksi) just exceeds the specified minimum material yield strength (135 ksi).

## Discussion

### Phase Transformation Temperatures

The phase transformation temperatures reported here for the 15Cr-135 SMSS alloy are useful in designing PWHT conditions. Here, we compare our findings to previous studies. Our reported $A_1$ temperature of 570°C at a heating rate of 0.0567 °C $s^{-1}$ and our measured reduction in yield strength (shown in Table 3 and Fig. 7A) from 145 ksi (as-received 15Cr-135 SMSS alloy) to 123 ksi with 1 h heat treatment at 621°C are in good agreement with the hardness reduction reported in Fig. 3 and reported changes in austenite fraction and yield strength by Ishiguro et al. (Ref. 10). The changes in hardness reported by Barbosa et al. in 15Cr-5.8Ni-1.9Mo-1Cu alloy (Ref. 21) and by Ye et al. in a 14.8Cr-6.5Ni-2Mo-1.4Cu-0.8W-0.021C alloy (Ref. 22) for various heat treatment conditions are all in good agreement with the hardness reduction in the base metal that we report in Fig. 4B and support the identified $A_1$ phase transformation temperature. While Ye et al. conclude that the $A_1$ temperature is below 550°C in a 14.8Cr-6.5Ni-1.8Mo-1.45Cu-0.021C alloy (Ref. 23), the increased Cu will likely stabilize austenite (e.g., see Ye et al. comparing austenite fraction for 1.44 and 2.74% Cu [Ref. 22]) and may lower the $A_1$ compared to the alloy investigated here with 0.95 wt-% Cu. Finally, the heating rate dependence of the austenite start and finish temperatures have been previously reported in both martensitic steels (Ref. 33) and stainless steel materials (Ref. 24). In a 13Cr-7Ni-3Si martensitic stainless steel, Leem et al. reports that the $A_1$ and $A_3$ transformation temperatures were nearly independent of heating rate at rates above 10°C $s^{-1}$ (Ref. 24). Apple and Krauss (Ref. 34) suggest a diffusional transformation mechanism below that rate and a diffusionless (shear) mechanism above it. We find that the heating rate dependence in this work is well-described by a linear fit between the transformation temperature and the logarithm of the heating rate (see Fig. 1D). Taken together, previous studies are in good agreement

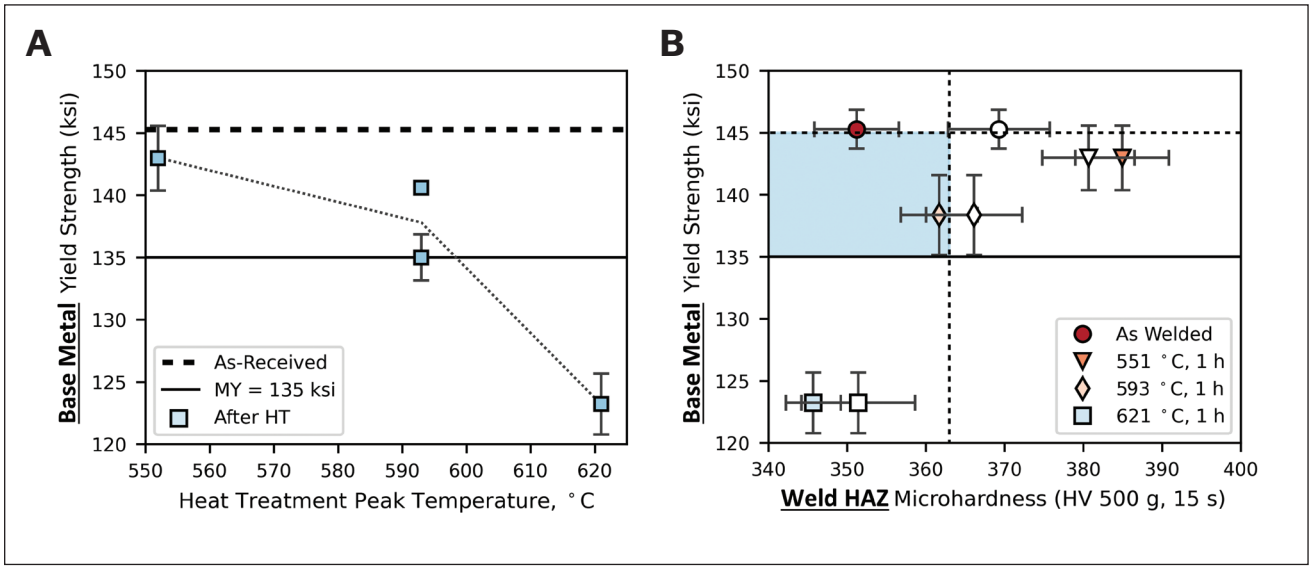


*Fig. 7 — A — 15Cr-135 alloy base metal yield strength (YS) measured after tempering at the indicated temperature for 1 h. Thick, dashed line is the as-received base metal YS. The thin, solid line is the specified minimum YS (135 ksi); B — measured base metal YS plotted versus weld HAZ microhardness at 0.25 mm from FZ line (filled symbols) and 1.75 mm from FZ (open symbols) for equivalent temperatures for base metal HT and weld PWHT. Thin, vertical line (363 HV) is the target maximum 37 HRC hardness limit. In (B), the thin, solid line is the specified minimum YS (135 ksi), and the thin, dashed line is the specified material maximum YS (145 ksi).*

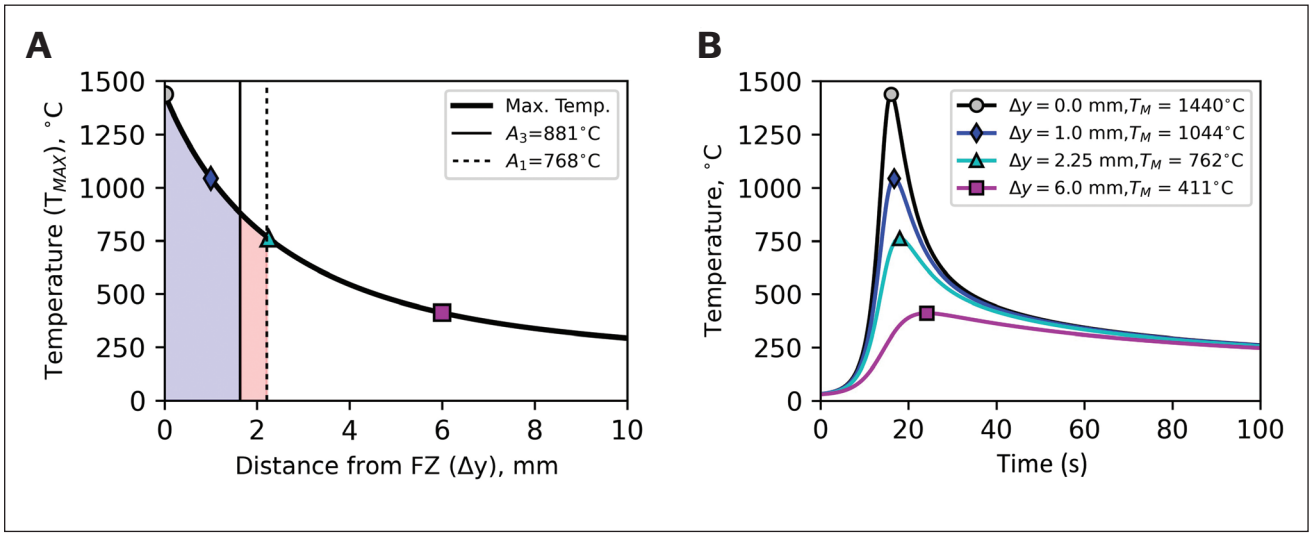


*Fig. 8 — A — Simulated maximum temperature in the HAZ ($T_{MAX}$) as a function of distance (Δy) from the weld fusion zone (FZ) boundary for the 15Cr SMSS BOP weld using the Rosenthal MPT model; B — simulated transient response at points indicated in (A) at Δy of 0, 1, 2.25, and 6 mm.*

with the phase transformation behavior reported in this work for the 15Cr-135 SMSS alloy.

## Temperature Distribution in Weld HAZ

To better understand the origin of microstructural heterogeneity in the HAZ, the BOP weld temperature was simulated using a distributed point source solution to the medium plate thickness (MPT) Rosenthal heat flow calculation for welding (Ref. 35), following the method of images previously reported (Refs. 36–38). The code was implemented in Python (version 3.9.12) and benchmarked to literature results (Ref. 37). The model welding parameters are the same as the BOP weld — 11 V, 120 A, and travel speed of 2.64 in./min (1.1176 mm/s) — with an arc efficiency of 0.7, which is similar to literature values (e.g., 0.74 in. [Ref. 39]). A uniform distribution of 3 heat sources was used on the simulated plate surface (thickness of 11.07 mm), normal to the weld direction at –1, 0, and 1 mm and centered at the weld origin. The thermal conductivity, κ

**Table 4 — Tensile Properties as Determined from Testing According to ASTM A370 (Ref. 31) with 0.250 in. (6.4 mm) Reduced Section**

| Condition | Number of Samples | Ultimate Tensile Strength, ksi | | Yield Strength, ksi | | Elongation, % | | Reduction of Area, % | |
|---|---|---|---|---|---|---|---|---|---|
| | | Avg. | Standard Deviation | Avg. | Standard Deviation | Avg. | Standard Deviation | Avg. | Standard Deviation |
| As-Received | 3 | 150.5 | 0.7 | 145.3 | 1.6 | 25.0 | 1.0 | 69.3 | 3.1 |
| 552°C, 1 h | 2 | 151.1 | 0.6 | 143.0 | 2.6 | 25.0 | 0.0 | 71.5 | 0.7 |
| 593°C, 1 h | 3 | 149.3 | 0.8 | 140.6 | 0.2 | 23.7 | 0.6 | 72.0 | 0.0 |
| 593°C, 1 h | 2 | 145.9 | 0.8 | 135.0 | 1.9 | 25.5 | 0.7 | 71.0 | 0.0 |
| 621°C, 1 h | 2 | 140.8 | 3.2 | 123.2 | 2.4 | 27.5 | 0.7 | 72.5 | 0.7 |

*A replicate heat treatment was performed at 593°C, so average tensile results are listed separately.

= 19.4 [W/(m K)], and the thermal diffusivity, $\alpha = 4.19 \times 10^{-6}$ [$m^2/s$], were found by averaging between 25 to 800°C of the temperature-dependent thermal properties reported for a 15-5PH powder material by Fang et al. (Ref. 40), which we expect to show similar thermal properties to the 15Cr-135 SMSS alloy investigated here. The liquidus temperature was taken to be 1440°C.

Using the MPT model, the fusion zone (FZ) was predicted to be 7.66 mm wide and 3.61 mm deep while the average experimental weld width and depth were measured to be 7.34 ± 0.11 and 1.47 ± 0.06 mm, respectively. While the model overestimates the FZ depth, the reasonable agreement to the weld width suggests that the model can be used to analyze the thermal cycle along the plate surface, roughly corresponding to the hardness traverse location indicated in Fig. 2A. Therefore, the maximum temperature was computed on the simulated plate surface, normal to the welding direction, as a function of distance ($\Delta y$) from the FZ boundary (i.e., the point where the simulated maximum temperature equals the liquidus temperature). The result of this analysis is presented in Fig. 8A, where the maximum HAZ temperature ($T_{MAX}$) is plotted as a function of $\Delta y$. The transient response of the material at $\Delta y = 0$, 1, 2.25, and 6 mm is presented in Fig. 8B. For $\Delta y$ of 1 and 2.25 mm, the heating rate between 250 °C and the peak temperatures was found to be 144°C $s^{-1}$ and 83 °C $s^{-1}$, respectively. Using the heating rate dependent $A_3$ and $A_1$ relations presented in Fig. 1D, the $A_3$ and $A_1$ are calculated to be 881 and 768°C, respectively, and the predicted positions with this peak temperature are superimposed on Fig. 8A as thin solid and dashed lines.

## Origin of Microstructural Heterogeneity in HAZ

In the 30 kJ/in. autogenous GTA bead-on-plate weld reported here, the HAZ will experience rapid heating and cooling. As indicated by the blue shaded region in Fig. 8A, the HAZ within $\Delta y = 1.64$ mm of the FZ is predicted to have a peak HAZ temperature that exceeds the predicted $A_3$ temperature. Consistent with this predicted temperature, microscopy suggests that the original base metal microstructure of martensite and reverted austenite (Fig. 5C) does experience austenitization, some grain growth, and formation of an as-quenched martensitic structure at $\Delta y = 0.5$ mm, as shown in the microstructure in Fig. 5D. Since the estimated martensite finish temperature is below room temperature, this region may not be fully martensitic. The microstructure found in the as-welded HAZ at $\Delta y = 1$ mm shows some evidence of reverted austenite, but it is closer to the as-quenched microstructure at $\Delta y = 0.5$ mm (Fig. 5D) than that seen at $\Delta y = 2$ mm (Fig. 5F), suggesting it experienced a peak temperature just at or above the $A_3$ temperature, consistent with the simulated temperature response in Fig. 8. Finally, the evident increase in austenite in the as-welded image $\Delta y = 2$ mm from the FZ boundary (Fig. 5F) is consistent with heating into an intercritical temperature range, as predicted by the simulated temperature response (Fig. 8; see red shaded area). In this analysis, the presence of light-etching morphologies is presumed to be austenite (Figs. 5D–F), in line with previous studies of SMSS alloys (e.g. [Ref. 18]).

While the simulated temperature distribution (Fig. 8) is consistent with the formation of reverted austenite, at $\Delta y = 2$ mm the *increased* austenite content is expected to correlate to *decreased* hardness (Ref. 22). However, as shown in Fig. 4A, *higher* hardness is found between 1.5–2.0 mm from the FZ boundary. Considering the previous investigations of the 15Cr SMSS alloy system have revealed the important role of nanoscale Cu-rich precipitates in alloy strengthening (Refs. 22, 23, 26), we hypothesize that sub-micron changes to material microstructure, such as precipitate volume fraction and dislocation density, are caused by welding heat flow and result in the measured changes in microhardness. Subsequent PWHT causes further changes in microhardness (Fig. 3)

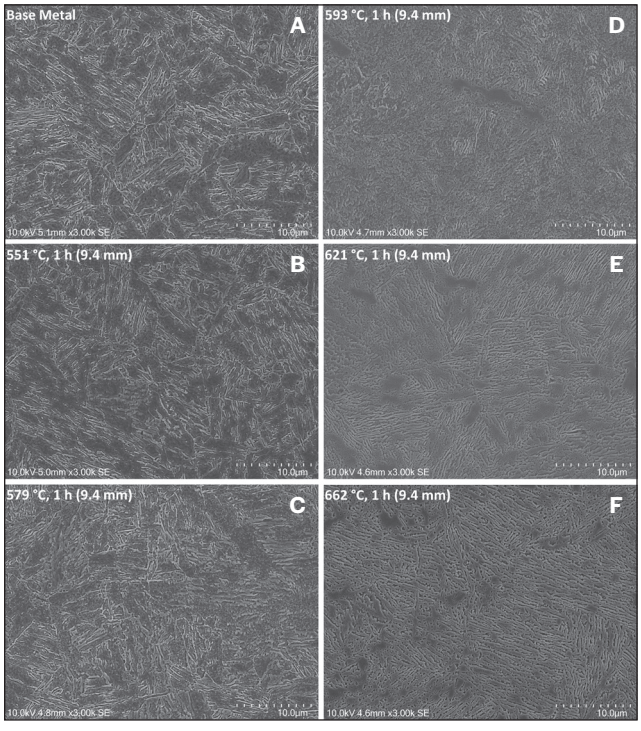


*Fig. 9 — Scanning electron microscopy (3,000×) of 15Cr-135 SMSS: A — Base metal. Region 9.4 mm from FZ boundary at indicated postweld heat treatment of: B — 551; C — 579; D — 593; E — 621; and F — 622 °C for 1 h.*

and microstructure, as revealed in microscopy presented in Figs. 5–8. While the increased fraction of austenite accounts for HAZ hardness reductions (e.g., for PWHT at 621 °C for 1 h, see Figs. 6C and F and Fig. 4), the origin of hardening in the HAZ was not directly observed in this study at lower PWHT temperatures. Characterization of Cu-rich precipitates in 15Cr-5Ni systems has been previously reported with high-resolution transmission electron microscopy (TEM) (Refs. 22, 23), energy dispersive spectroscopy (EDS) (Ref. 22), and atom probe tomography (APT) (Refs. 26, 41), while the austenite volume fraction has been quantified by x-ray diffraction (e.g., see [Ref. 22]) and SEM electron-beam scattered diffraction (Ref. 25). Thermodynamic modeling has also been useful in revealing microstructure evolution in martensitic materials (e.g., see [Refs. 18, 41]). Application of these experimental and computational methods to confirm the hypothesized changes in microstructure, particularly the size and volume fraction of nanoscale precipitates, would be fruitful but was beyond the scope of the present investigation.

## Correlation of PWHT Condition in 15Cr Welds to Base Metal Properties

The overall reduction of yield strength shown in Table 4 and Fig. 7B agrees with the overall reduction in the microhardness measurements shown in Fig. 3. It is desirable to develop PWHT methods that both preserve minimum base metal yield strength while reducing HAZ hardness below acceptable limits. Accordingly, following our previously developed methodology (Ref. 14), in Fig. 7B we develop a design guide that plots the base metal yield strength versus the HAZ weld microhardness for equal heat treatment and postweld heat treatment temperatures, respectively. For reference, the 135 ksi minimum YS and 145 ksi maximum YS are plotted as thin solid and dashed horizontal lines, respectively, while the target maximum material hardness of 37 HRC (363 HV) is indicated as a thin vertical dashed line. Using this plot in Fig. 7B, the region in blue indicates the target combination of hardness less than 37 HRC and base material YS between 135 and 145 ksi. While the as-welded condition at first glance appears acceptable for CGHAZ hardness, the maximum hardness at 1.75 mm from the FZ falls outside the target region. By contrast, the PWHT condition of 593°C yields a HAZ hardness acceptable in the CGHAZ and close at 1.75 mm, while preserving the base metal YS above 135 ksi. This design guide demonstrates that in this high-strength, quench and tempered 15Cr-135 SMSS alloy system, PWHT for HAZ hardness reduction must be carefully selected to avoid reduction of base metal YS below specified material minimums.

The base metal microstructure was characterized for different heat treatment conditions by SEM imaging approximately 9.4 mm from the FZ boundary. As can be seen in Fig. 9, changes in base metal microstructure are negligible at heat treatment of 551 and 579°C for 1 h (Figs. 9B and C), consistent with minimal changes in base metal YS at 551°C (Fig. 7A). However, after heat treatment at 593°C for 1 h (Fig. 9D), the reverted austenite morphology changes from intragranular reverted austenite lamella to a less aligned, higher volume fraction of reverted austenite with some "islands" that resemble morphologies that have been previously identified as delta ferrite (Ref. 21). These changes in microstructure are even more pronounced at 621 and 662°C (Figs. 9E and F), correlating with the significant reduction in base metal YS measured at 621°C (Fig. 7A).

## Implications of HAZ Hardness for Welding Procedure Development

This work has two practical implications. First, the maximum hardness for the as-welded HAZ and after most PWHT conditions is at approximately 1.75 mm from the FZ boundary (Fig. 3). Therefore, microhardness measurements made in the CGHAZ immediately adjacent to the FZ boundary may not reflect the true maximum hardness in the HAZ. This finding is relevant for welding procedure design and qualification to standards such as NACE MR0175/ISO 15156 (Ref. 19). Second, the developed design guide (Fig. 7B) reveals that PWHT intended to promote corrosion resistance through HAZ hardness reductions may cause degradation to base alloy yield strength. As shown in Table 4, PWHT has a smaller impact on the ultimate tensile strength than on the yield strength, likely due to transformation-induced plasticity (TRIP) during deformation as reverted austenite transforms to martensite (e.g., see [Ref. 12]). If welding procedure qualification relies upon ultimate tensile strength, such as is outlined in ASME Section IX welding procedure qualification (Ref. 42), reductions to base metal yield strength may be undetected.

## Conclusions

From this work, the following conclusions may be drawn about 15Cr-6Ni-2Mo-1Cu supermartensitic stainless steel alloy with 135 ksi minimum yield:

- The austenite start ($A_1$) and finish ($A_3$) temperatures are found to be heating rate dependent, with values of 570 and 713°C (respectively) predicted for heating rates of 0.0567°C $s^{-1}$. The martensite start temperature is found to be 95.5°C.
- Autogenous gas tungsten arc (GTA) bead-on-plate (BOP) welds result in heterogeneity in the as-welded heat-affected zone, as reflected by spatially varying microhardness and microstructure, with a maximum hardness of 1.75 mm from the fusion zone boundary that exceeds the maximum base metal hardness.
- Postweld heat treatment (PWHT) of autogenous GTA welds causes significant HAZ hardening for PWHT temperatures below the predicted $A_1$ temperature of 570°C, while PWHT at temperatures above 593°C is correlated to significant reductions in base metal hardness and yield strength.
- A design guide is developed that compares the effect of PWHT on HAZ hardness and base metal yield strength and demonstrates that PWHT at 593°C may offer the best compromise of HAZ hardness reduction and preservation of base metal yield strength in this alloy above 135 ksi.

### *Acknowledgments*

We thank D. Stolk for assistance with tensile testing and the W. M. Keck Foundation for supporting the purchase of the SEM instrument. Financial support for the research performed at LeTourneau University was provided by Halliburton. Initial experimental work peformed by Reed Phillips is gratefully acknowledged.

### *References*

1. Kimura, M., Miyata, Y., Toyooka, T., and Kitahaba, Y. 2001. Effect of retained austenite on corrosion performance for modified 13% Cr steel pipe. *Corrosion* 57: 433–439. DOI: 10.5006/1.3290367.

2. Lippold, J. C., and Kotecki, D. J. 2005. Welding metallurgy and weldability of stainless steels. New Jersey, Wiley.

3. Zou, D., Han, Y., Zhang, W., and Fang, X.-D. 2010. Influence of tempering process on mechanical properties of 00Cr13Ni4Mo supermartensitic stainless steel. *Journal of Iron and Steel Research International* 17: 50–54. DOI: 10.1016/S1006-706X(10)60128-8.

4. Gooch, T. G. 1995. Heat treatment of welded 13% Cr-4% Ni martensitic stainless steels for sour service. *Welding Journal* 74: 213-s.

5. Ramirez, J. E. 2007. Weldability evaluation of supermartensitic stainless pipe steels, *Welding Journal* 86: 125-s–134-s.

6. Zappa, S., Svoboda, H., Ramini, M., Rissone, N., Surian, E., and Vedia, D. 2012. Improving supermartensitic stainless steel weld metal toughness. *Welding Journal* 91: 83-s.

7. Woollin, P. 2007. Understanding and avoiding intergranular stress corrosion cracking of welded supermartensitic stainless steel. *NACE Corrosion Conference Papers*. NACE International.

8. Skar, J. I., and Olsen, S. 2015. Super Martensitic Stainless Steel and Sour Service–Testing and Evaluations. *NACE Corrosion Conference Papers*. NACE International.

9. Kimura, M., Tamari, T., Yamazaki, Y., Sakata, K., Mochizuki, R., and Sato, H. 2005. Development of new 15Cr stainless steel OCTG with superior corrosion resistance. *SPE High Pressure/High Temperature Sour Well Design Applied Technology Workshop*. Society of Petroleum Engineers. DOI: 10.2118/98074-MS.

10. Ishiguro, Y., Eguchi, K., Fujimura, K., and Nakahashi, T. 2016. Electrochemical analyses of 15% Cr and 17% Cr martensite-based stainless steel OCTG materials with a possible range of austenite ratio. *NACE International Corrosion Conference Proceedings*. NACE International.

11. Tavares, S. S. M., Almeida, B. B., Corrêa, D. A. L., and Pardal, J. M. 2018. Failure of super 13Cr stainless steel due to excessive hardness in the welded joint. *Engineering Failure Analysis* 91: 92–98. DOI: 10.1016/j.engfailanal.2018.04.018.

12. Bilmes, P. D., Solari, M., and Llorente, C. L. 2001. Characteristics and effects of austenite resulting from tempering of 13Cr–NiMo martensitic steel weld metals. *Materials Characterization* 46: 285–296. DOI: 10.1016/S1044-5803(00)00099-1.

13. Akselsen, O. M., Rorvik, G., Kvaale, P. E., and Van der Eijk, C. 2004. Microstructure-property relationships in HAZ of new 13% Cr martensitic stainless steels. *Welding Journal* 83: 160–167.

14. Nam Vu, T., Krishnan, K., Sisk, J., Phillips, R., Wells, A., Hill, S., Gabbert, K., and Baumer, R. E. 2021. Welding procedure development for a 13Cr-5Ni-2Mo (UNS S41426) super martensitic stainless steel. *NACE International Corrosion Conference Proceedings*. NACE-2021-16840.

15. Da Silva, G. F., Tavares, S. S. M., Pardal, J. M., da Silva, M. R., and De Abreu, H. F. G. 2011. Influence of heat treatments on toughness and sensitization of a Ti-alloyed supermartensitic stainless steel. *Materials Research* 46: 7737–7744. DOI: 10.1590/1980-5373-mr-2016-0409.

16. Escobar, J. D., Faria, G. A., Wu, L., Oliveira, J. P., Mei, P. R., and Ramirez, A. J. 2017. Austenite reversion kinetics and stability during tempering of a Ti-stabilized supermartensitic stainless steel: Correlative in situ synchrotron x-ray diffraction and dilatometry. *Acta Materialia* 138: 92–99. DOI:10.1016/j.actamat.2017.07.036.

17. Escobar, J. D., Oliveira, J. P., Salvador, C. A. F., Faria, G. A., Poplawsky, J. D., Rodriguez, J., Mei, P. R., Babu, S. S., and Ramirez, A. J. 2018. Meta-equilibrium transition microstructure for maximum austenite stability and minimum hardness in a Ti-stabilized supermartensitic stainless steel. *Materials & Design* 156: 609–621. DOI: 10.1016/j.matdes.2018.07.018.

18. Escobar, J. D., Oliveira, J. P., Salvador, C. A. F., Tschiptschin, A. P., Mei, P. R., and Ramirez, A. J. 2019. Double-step inter-critical tempering of a supermartensitic stainless steel: Evolution of hardness, microstructure and elemental partitioning. *Materials Characterization* 158: 109994. DOI: 10.1016/j.matchar.109994.

19. NACE MR0175/ISO 15156. 2015. Petroleum and natural gas industries-Materials for use in H2S-containing environments in oil and gas production. NACE: Houston, TX.

20. Wilms, M. E., de Jong, J., Majoor, J. C. J. E., and Huizinga, S. 2013. TEM investigations into the effect of PWHT on IGSCC susceptibility of weldable 13cr linepipe. *Corrosion 2013*. NACE International.

21. Barbosa, B., Tavares, S., Bastos, I., Silva, M., and de Macedo, M. 2014. Influence of heat treatments on microstructure and pitting corrosion resistance of 15% Cr supermartensitic stainless steel. *Corrosion Engineering, Science and Technology* 49(4): 311–315. DOI: 10.1179/1743278214Y.0000000156.

22. Ye, D., Li, J., Jiang, W., Su, J., and Zhao, K. 2012. Effect of Cu addition on microstructure and mechanical properties of 15% Cr super martensitic stainless steel. *Materials & Design* 41: 16–22. DOI: 10.1016/j.matdes.2012.04.036.

23. Ye, D., Li, J., Jiang, W., Su, J., and Zhao, K. 2013. Formation of reversed austenite in high temperature tempering process and its effect on mechanical properties of Cr15 super martensitic stainless steel alloyed with copper. *Steel Research International* 84: 395–401. DOI:10.1002/srin.201200105.

24. Leem, D. -S., Lee, Y. -D., Jun, J. -H., and Choi, C. -S. 2001. Amount of retained austenite at room temperature after reverse transformation of martensite to austenite in an Fe–13%Cr–7%Ni–3%Si martensitic stainless steel. *Scripta Materialia* 45: 767–772. DOI: 10.1016/S1359-6462(01)01093-4.

25. Zhou, T., Faleskog, J., Babu, R. P., Odqvist, J., Yu, H., and Hedström, P. 2019. Exploring the relationship between the microstructure and strength of fresh and tempered martensite in a maraging stainless steel Fe–15Cr–5Ni. *Materials Science and Engineering A* 745: 420–428. DOI: 10.1016/j.msea.2018.12.126.

26. Couturier, L., De Geuser, F., Descoins, M., and Deschamps, A. 2016. Evolution of the microstructure of a 15-5PH martensitic stainless steel during precipitation hardening heat treatment. *Materials & Design* 107: 416–425. DOI: 10.1016/j.matdes.2016.06.068.

27. ASTM. 2007. E140-07 Standard hardness conversion tables for metals relationship among brinell hardness, vickers hardness, rockwell hardness, superficial hardness, knoop hardness, and scleroscope hardness. *ASTM International*, West Conshohocken, Pa. ASTM. 1–21. DOI: 10.1520/E0140-07.

28. Barrick, E. J., and DuPont, J. N. 2019. Mechanical properties and microstructural characterization of simulated heat-affected zones in 10 wt pct Ni steel. *Materials Science and Engineering A* 748: 189–204. DOI: 10.1016/j.msea.2019.01.085.

29. ASME. 2015. BPVC Section VIII-Rules for Construction of Pressure Vessels Division 3-Alternative Rules for Construction of High-Pressure Vessels. 1: 1.

30. ASTM. 2017. E384-17: Standard test method for microindentation hardness of materials. *ASTM International*, West Conshohocken, Pa. DOI: 10.1520/E0384-17.

31. ASTM. 2019. A370-19e1: Standard test methods and definitions for mechanical testing of steel products. *ASTM International*, West Conshohocken, Pa. DOI: 10.1520/A0370-19E01.

32. Bhadeshia, H., and Honeycombe, R. 2017. Steels – Microstructure and Properties. *Butterworth-Heinemann* 4th Ed. DOI: 10.1016/B978-0-08-100270-4.00026-3.

33. Barrick, E. J., Jain, D., DuPont, J. N., and Seidman, D. N., 2017. Effects of heating and cooling rates on phase transformations in 10 wt pct Ni steel and their application to gas tungsten arc welding. *Metallurgical and Materials Transactions A* 48: 5890–5910. DOI: 10.1007/s11661-017-4379-0.

34. Apple, C.A., and Krauss, G., 1972. The effect of heating rate on the martensite to austenite transformation in Fe-Ni-C alloys. *Acta Metallurgica* 20(7): 849–856. DOI: 10.1016/0001-6160(72)90077-6.

35. Rosenthal, D., 1946. The theory of moving sources of heat and its application to metal treatments. *Transactions ASME* 68: 849–865.

36. Grong, Ø., 1997. Metallurgical modelling of welding. *Institute of Materials, London* 2: 77-80.

37. Ramirez, A. J., and Brandi, S. D., 2004. Application of discrete distribution point heat source model to simulate multipass weld thermal cycles in medium thick plates. *Science and Technology of Welding & Joining* 9: 72–82. DOI: 10.1179/136217104225017189.

38. Ferreira, D. M., Alves, A. D., Cruz Neto, R. M., Martins, T. F., and Brandi, S. D., 2018. A new approach to simulate HSLA steel multipass welding through distributed point heat sources model. *Metals* 8. DOI: 10.3390/met8110951.

39. Fujiyama, S., Shigeta, M., and Tanaka, M., 2021. Comparison between methods measuring arc efficiency of gas tungsten arc welding. *Science and Technology of Welding and Joining* 26: 371–376. DOI: 10.1080/13621718.2021.1921101.

40. Fang, J. X., Dong, S. Y., Wang, Y. J., Xu, B. S., Zhang, Z. H., Xia, D., He, P., 2015. The effects of solid-state phase transformation upon stress evolution in laser metal powder deposition. *Materials & Design* 87: 807–814. DOI: 10.1016/j.matdes.2015.08.061.

41. Zhou, T., Neding, B., Lin, S., Tseng, J.-C., and Hedström, P. 2021. Cu precipitation-mediated formation of reverted austenite during ageing of a 15–5 PH stainless steel. *Scripta Materialia* 202: 114007. DOI: 10.1016/j.scriptamat.2021.114007.

42. ASME. 2017. *BPVC Section IX-Welding, Brazing, and Fusing Qualifications*, New York.

**RICHARD E. BAUMER** is with the Department of Aerospace, Industrial and Mechanical Engineering, California Baptist University, Riverside, Calif. **EZEQUIEL CAIRES PEREIRA PESSOA** (*ezequielpessoa@letu.edu*) is with the Department of Welding/Materials Joining Engineering, LeTourneau University, Longview, Tex. **KARTHIK KRISHNAN** is with Halliburton Energy Service, Carrollton, Tex. **THANH NAM VU** is with Halliburton Completion Technology and Manufacturing Center, Singapore, Republic of Singapore.